



CHALMERS
UNIVERSITY OF TECHNOLOGY

CVD TiAlN coatings with tunable nanolamella architectures

Downloaded from: <https://research.chalmers.se>, 2024-03-13 06:55 UTC

Citation for the original published paper (version of record):

Qiu, R., Bäcke, O., Stiens, D. et al (2021). CVD TiAlN coatings with tunable nanolamella architectures. Surface and Coatings Technology, 413.
<http://dx.doi.org/10.1016/j.surfcoat.2021.127076>

N.B. When citing this work, cite the original published paper.



CVD TiAlN coatings with tunable nanolamella architectures

Ren Qiu^{a,*}, Olof Bäcké^a, Dirk Stiens^b, Wiebke Janssen^b, Johannes Kümmel^b, Thorsten Manns^b, Hans-Olof André^a, Mats Halvarsson^a

^a Department of Physics, Chalmers University of Technology, SE-41296 Gothenburg, Sweden

^b Walter AG, D-72072 Tuebingen, Germany

ARTICLE INFO

Keywords:

CVD
TEM
XRD
EBSD
TiAlN
Gas flow

ABSTRACT

In this work, $\text{Ti}_{1-x}\text{Al}_x\text{N}$ (TiAlN) coatings were synthesized by low pressure chemical vapour deposition (LPCVD), and the influence of a rotational precursor gas supply on the coating microstructure was studied. The microstructure of the TiAlN coatings were characterized using X-ray diffraction (XRD), scanning and transmission electron microscopy (SEM and TEM), and electron backscattered diffraction (EBSD). It is shown that a rotational precursor gas supply induces an oscillatory surface reaction, which causes a nanolamella architecture. When the gas beam directly hits the sample, the local gas flow velocity is high, which increases the deposition rate of Ti and a Ti(Al)N lamella is formed. When the gas beam rotates away, the local gas velocity is low, so the deposition rate of Ti decreases, and an Al(Ti)N lamella is formed. As this is repeated a periodic nanolamella architecture is formed. The nanolamellae grow epitaxially on three {001} facets of the 111 textured grains, which leads to a pyramidal surface morphology. Without gas supply rotation, a high Al content cubic phase was still obtained, but no nanolamella was formed. This indicates that Ti-rich lamellae are not necessary to stabilize an Al-rich cubic TiAlN phase. In addition, spinodal decomposition is not likely to be the driving force behind the nanolamella formation in LPCVD TiAlN, as this would also have happened in the sample without a rotational gas supply. Finally, the nanolamella periodicity is found to be tunable via controlling the rotation speed of the precursor supply relative to the coating growth rate.

1. Introduction

High-speed metal machining generates extreme pressures and thermal loads, which put high requirements on cutting tool materials, and requires both extraordinary hardness and fracture toughness [1]. Today cutting tool inserts are usually made of cemented carbides, which are often coated with wear-resistant coatings. It is a challenging task to synthesize new wear-resistant coatings that are optimized for machining the growing variety of workpiece materials that are used in modern industry. $\text{Ti}_{1-x}\text{Al}_x\text{N}$ (TiAlN) with rock-salt (B1) crystal structure exhibits outstanding mechanical properties and good chemical and thermal stabilities, and is thus a material that is widely used in the cutting tool industry [2,3]. The TiAlN coatings are most often deposited by Physical Vapour Deposition (PVD) [2,4,5]. In recent years, TiAlN with a high Al content ($x \sim 0.8$ in $\text{Ti}_{1-x}\text{Al}_x\text{N}$) has been synthesized by low pressure chemical vapour deposition (LPCVD), reaching levels of Al at present not possible with PVD without formation of considerable amounts of AlN with hexagonal structure [2,3,6–13]. Good thermal stability and hot

hardness for high Al content LPCVD TiAlN coatings have been reported, which indicates a promising application of this type of coatings for the cutting tool industry [6,7].

LPCVD TiAlN coatings have been reported to exhibit a nanolamella architecture, consisting of alternating Al-rich (Al(Ti)N) and Ti-rich (Ti(Al)N) lamellae [6–8,14]. What effect this architecture has on the mechanical properties of TiAlN coatings is not known. Possibly, the nanolamella architecture influences the mechanical properties of LPCVD coatings due to interfacial straining. Such architectures have been shown to, in some cases, tune the hardness and elastic modulus of materials, and the effect is varying with the periodicity of the nanolamella structure. This has been suggested to stem from factors such as strengthening from alternating interfacial stresses and dislocation strengthening due to the Hall-Petch effect [15–17]. PVD has been used extensively to deposit hard coatings with nanolamella architecture that have varying periodicities [2,18–22]. In comparison, it has been much more challenging to synthesize wear-resistant coatings with such a structure using CVD. However, CVD TiAlN coatings with nanolamella

* Corresponding author.

E-mail address: renq@chalmers.se (R. Qiu).

<https://doi.org/10.1016/j.surfcoat.2021.127076>

Received 13 December 2020; Received in revised form 8 March 2021; Accepted 10 March 2021

Available online 20 March 2021

0257-8972/© 2021 The Authors. Published by Elsevier B.V. This is an open access article under the CC BY license (<http://creativecommons.org/licenses/by/4.0/>).

architecture can now be synthesized [6–8,23], but what drives the formation of this architecture in LPCVD TiAlN coatings is not yet fully understood. This understanding is essential for controlling and tuning the nanolamella architecture, such as lamella periodicity, and thereby tune the mechanical properties of the coatings.

Different mechanisms have been proposed to explain the formation of the nanolamella architecture in LPCVD TiAlN. Paseuth, et al. proposed that spinodal decomposition is what drives the formation of the nanolamellae [23]. However, Zalesak, et al. argued that the nanolamella architecture instead forms due to some oscillatory chemical reactions, which are kinetically controlled and causes a self-assembly process to form the Ti(Al)N and the Al(Ti)N lamellae [6]. In our previous work, a rotational gas supply was used for LPCVD synthesis of TiAlN coatings [7]. These coatings had a nanolamella structure that was influenced by the local flow rate, and by keeping the flow rate low a well-defined periodic nano-structure was obtained. Periodic variations in the local chemical environment, including flow velocity, due to a constantly rotating gas supply of precursors can thus also be a reason behind the formation of the Al-rich and the Ti-rich nanolamellae. This hypothesis is tested in this paper. By varying the rotation speed of the gas supply, the nanolamella periodicity in the LPCVD TiAlN is expected to change.

In order to investigate whether there is a correlation between the rotational gas supply and the nanolamella architecture, we have in this work synthesized three different TiAlN coatings with different rotation speeds for the gas supply. The influence on the coating microstructure, including different nanolamella architectures, texture, grain morphology and chemical composition, is investigated using scanning and transmission electron microscopy (SEM and TEM), electron back-scattered diffraction (EBSD), X-ray energy dispersive spectrometry (XEDS) and X-ray diffraction (XRD).

2. Materials and methods

2.1. LPCVD synthesis

TiAlN coatings were deposited in an industrial scale hot wall CVD equipment having a cylindrical reactor with overall dimensions of 1000 mm height and 300 mm diameter heated by a hood-type furnace. The area inside the reactor to be charged with substrates was about 750 mm in height and 275 mm in diameter (reaction zone). Gas flow through the reaction zone had radial geometry, the reactive gases and carrier gases being ejected from a central gas distribution pipe with an outer diameter of 45 mm rotating at variable speeds and being evacuated towards the vacuum pump system at the periphery.

Cemented carbide (94 wt% WC and 6 wt% Co) substrates of SNMA120404 geometry according to ISO 1832 (approximately 13 mm wide and 5 mm thick) were polished and cleaned with ethanol prior to deposition. The gases used for the deposition process had purities better than 99.99%. TiCl_4 was purchased from Cristal Global with 99.95% purity and evaporated. Aluminum chloride was generated in situ by reaction of Al pellets with gaseous HCl at temperatures of 300–400 °C. Under these conditions, it is a good approximation to assume 100% yield of the chlorination reaction. AlCl_3 as the predominant reaction product under the used conditions is considered as the active aluminum precursor for the purposes of our discussions, even though minor amounts of the dimer Al_2Cl_6 may be present in the equilibrium gas phase (see also reference [14]).

The cemented carbide substrates were pre-coated with a thin TiN layer at a temperature of 850 °C, under a pressure of 150 mbar, with TiCl_4 , N_2 and H_2 as precursors. The TiAlN coatings (samples A, B, and C) were grown using a AlCl_3 – TiCl_4 – NH_3 precursor system via different LPCVD recipes, at temperatures in the range from 650 to 750 °C, and pressures between 5 and 25 mbar. The samples which were used for this study were taken from positions at the bottom part of the reaction zone, within the lower 200 mm of usable height and within 40–120 mm radial distance from the gas distribution pipe. For more details of the sample

synthesis, see patent [24]. Table 1 gives the gas supply rotation speed (ω in revolution per minute (rpm)) and the coating growth rate v ($\mu\text{m}/\text{min}$) of coatings studied in this work.

2.2. XRD methods

For the determination of the coating phases a symmetrical θ - 2θ scan within the angle range of $30^\circ \leq 2\theta \leq 90^\circ$ with 0.026° step size was conducted using a Panalytical Empyrean Diffractometer with $\text{Cu K}\alpha$ -radiation run at 40 kV and 40 mA and with a PIXcel1D detector. In the incident beam path, Soller slits with 0.04 rad divergence, a fixed incident beam mask with 5 mm width, a 0.5° divergence slit and a 1° anti-scatter slit were used. In the diffracted beam path, a Ni $\text{K}\beta$ filter, Soller slits with 0.04 rad divergence and a 4° anti-scatter slit were used.

2.3. Electron microscopy experiments

SEM was used to study cross sections and top surfaces of the different coatings using a Zeiss Supra 40 VP instrument, with an in-lens detector and a standard secondary electron (SE) detector. Thin foil lift-out samples of the coatings for TEM characterizations were prepared using an FEI Versa 3D focused ion beam (FIB)-SEM equipment with an Omniprobe micromanipulator. Scanning transmission electron microscopy (STEM) was performed to study the detailed microstructure of the TiAlN coatings using an FEI Titan 80–300 TEM/STEM instrument with high angle annular dark field (HAADF) and bright field (BF) detectors. XEDS data was collected using an Oxford X-sight detector. EBSD was performed on coating cross sections polished by FIB-SEM. The EBSD measurements were done using a TESCAN GAIA3 FIB-SEM equipped with an Oxford NanoNordlys detector. The EBSD data was analyzed by Oxford HKL Channel 5 software.

3. Results

3.1. LPCVD TiAlN coated cemented carbide cutting tool insert

The TiAlN coatings were successfully deposited onto the cemented carbide inserts. Cross sections of the coatings were investigated using SEM. Fig. 1(a) is an SEM SE micrograph showing an overview of a cross section of one of the corners of sample A (synthesized by slow gas supply rotation). Both the flank and rake faces are coated with a TiAlN layer with uniform thickness ($\sim 6 \mu\text{m}$), showing a low porosity and low crack density. As shown by the higher magnification cross section micrograph in Fig. 1(b), the coating mainly consists of columnar grains. The SEM in-lens SE micrograph with even higher magnification, shown in Fig. 1(c), shows that the columnar grains are built up of a nanolamella structure.

The mean content of Al and Ti of all three samples (A, B, and C) was measured by XEDS, and was found to be approximately the same, see Table 1. The Cl content in all samples was found to be below the detection limit ($\sim 0.1 \text{ at. } \%$), and is not given in the table. The N content cannot be measured due to overlap of the N $\text{K}\alpha$ (392 eV) peak with the Ti $\text{L}\alpha$ (452 eV) peak.

Table 1

Growth rate (v), gas supply rotation speed (ω), and mean Al and Ti contents measured by XEDS for the TiAlN coatings. The errors are estimated to be less than 2% for the Ti and Al ratios.

Sample	A	B	C
v [$\mu\text{m}/\text{min}$]	0.023	0.217	0.073
ω [rpm]	0.5	0	5
Al/(Al + Ti)	77%	86%	83%
Ti/(Al + Ti)	23%	14%	17%

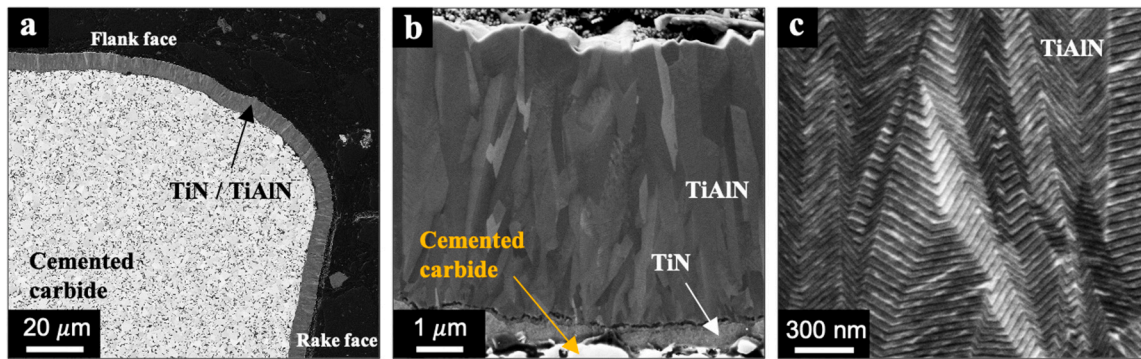


Fig. 1. SEM micrographs of TiAlN coating (sample A) cross section. (a) SE image of the cross section of one of the corners of the coated cutting tool insert. (b) SE image of the columnar structure of the coating. (c) In-lens SE micrograph of the lamella internal structure of the coating.

3.2. Coating texture and nanolamella orientation

XRD measurements were performed on coating A, and the θ - 2θ diffractogram is presented in Fig. 2. An intense 111 peak and a strong 222 peak of the TiAlN phase are identified in the diffractogram, indicating a strong 111 texture. It agrees with the cross section EBSD results, as shown in Fig. 3. According to the inverse pole figure (IPF) map and the corresponding colour map, see Fig. 3(a) and (b), the TiAlN grains grow in a columnar way with strong 111 texture, which is also confirmed by the {100}, {110}, and {111} pole figures, shown in Fig. 3(c), (d), and (e). (The slight deviation from 111 texture stems from the difficulty to mount small SEM specimens exactly parallel to the macroscopic insert surface.) In the X-ray diffractogram, apart from the peaks from the substrate (WC and W_6Co_6C) and the TiN layer, only peaks from face centered cubic (FCC) TiAlN phase were found. No peak from hexagonal AlN (h-AlN) above the background level could be observed. It is worth noting that a small amount of the co-grown h-AlN phase can exist at the grains boundaries of the TiAlN grains or inside the TiAlN grains, following a specific crystallographic orientation relationship, as was revealed in our previous publication [7]. However, the existence of the h-AlN phase cannot be identified in the X-ray diffractogram due to the limited amount.

The surface morphology of the LPCVD TiAlN coating (sample A) exhibits pyramidal structures, as seen in Fig. 4(a). It indicates that the 111 textured columnar grains form by growth of facets with a 3-fold rotational symmetry along the [111] direction. As illustrated by the 111 stereographic projection in Fig. 4(b), candidates of atomic planes of the grown facets can belong either to the {011}, {001}, or {111} planes, as marked by blue, red, and yellow spots, respectively. This will be investigated further below.

The detailed microstructure of the TiAlN sample A is shown as STEM results in Fig. 5. The columnar grains exhibit a nanolamella architecture, see the STEM HAADF micrograph in Fig. 5(a). According to the line profile measured along the nanolamella normal direction from the STEM HAADF image, the periodicity of the nanolamellae is around 33 nm. Z contrast STEM HAADF imaging suggests that the nanolamellae consist of thin Ti-rich (brighter) and thick Al-rich (darker) layers. This is confirmed by the STEM XEDS linescan, shown in Fig. 5(b), where the compositions of the Ti(Al)N and the Al(Ti)N lamellae are $Ti_{0.50}Al_{0.50}N$ and $Ti_{0.11}Al_{0.89}N$, respectively (nitrogen was not measured so stoichiometry with respect to N is assumed). High resolution STEM (HRSTEM) HAADF imaging reveals more details of the nanolamella architecture, as shown in Fig. 6(a). The Ti(Al)N lamellae have a thickness of around 3 nm, and since the total thickness is 33 nm (Fig. 5(a)), the Al(Ti)N lamellae are therefore around 30 nm. A fast Fourier transform (FFT) of the HRSTEM micrograph was calculated and is presented in Fig. 6(b), which indicates a cube-on-cube epitaxial growth of the Ti(Al)N and Al(Ti)N lamellae with the following crystallographic orientation relationship:

$$(001)_{Ti(Al)N} // (001)_{Al(Ti)N}, [010]_{Ti(Al)N} // [010]_{Al(Ti)N}.$$

3.3. Influence of precursor supply on nanolamella architecture

To investigate the influence of the precursor supply on the nanolamella architecture, another deposition was made, this time still using a radial flow reactor setup, but without rotation of the gas supply (sample B). The TiAlN coating on sample B also exhibits a pyramidal surface morphology, see Fig. 7(a). XRD measurements were also performed on coating B. The θ - 2θ diffractogram is shown in Fig. 8. An intense 111 peak

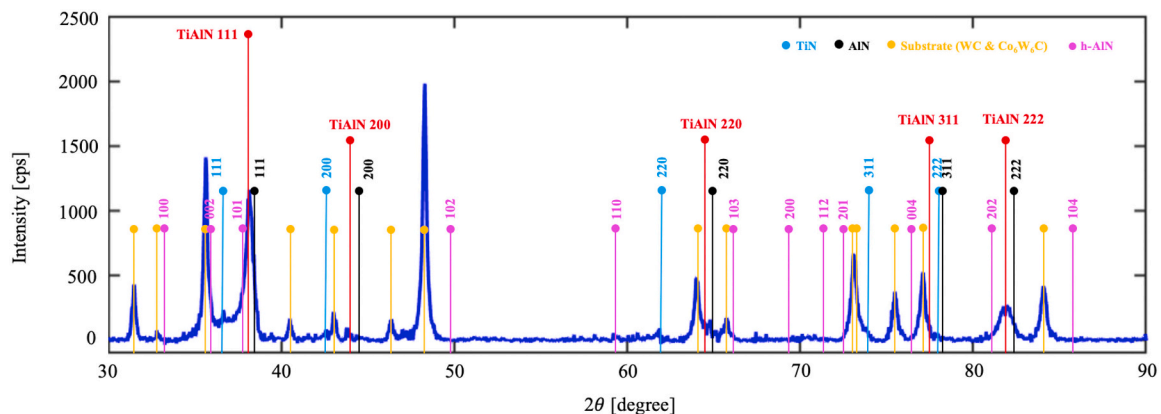


Fig. 2. X-ray diffractogram from sample A. The marked phases are (cubic) TiN (PDF 01-074-8388), (cubic) AlN (PDF 00-046-1200), WC (PDF 01-089-2727), and Co_6W_6C (PDF 00-022-0597). Location of peaks from h-AlN (PDF 00-025-1133) are marked for reference.

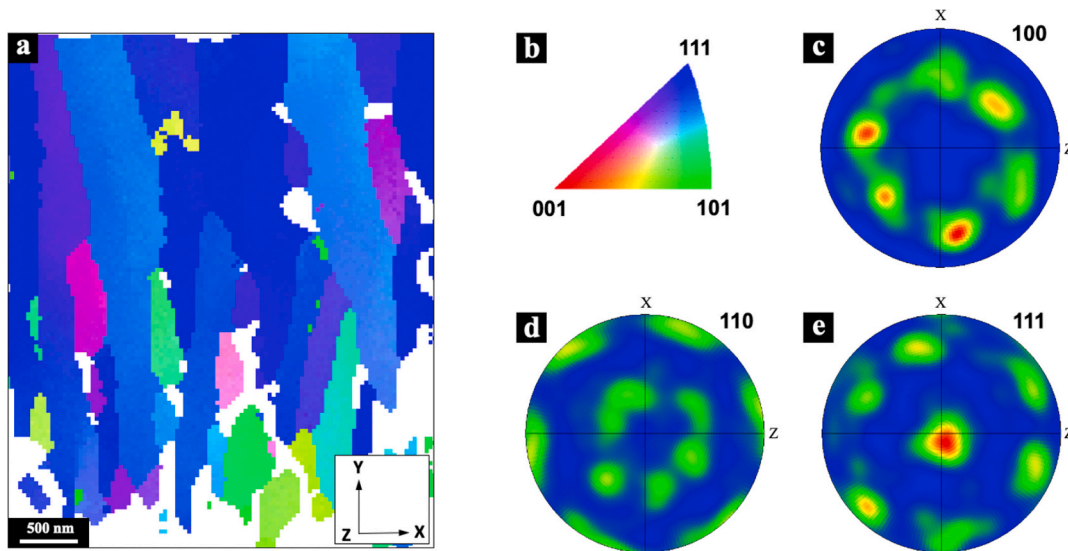


Fig. 3. Cross section EBSD results of sample A. (a) IPF map of the coating cross section along the coating growth direction (vertically) showing the 111 texture. (b) Colour legend for the IPF map. (c–e) {100}, {110}, and {111} pole figures viewed along the coating growth direction, confirming the 111 texture.

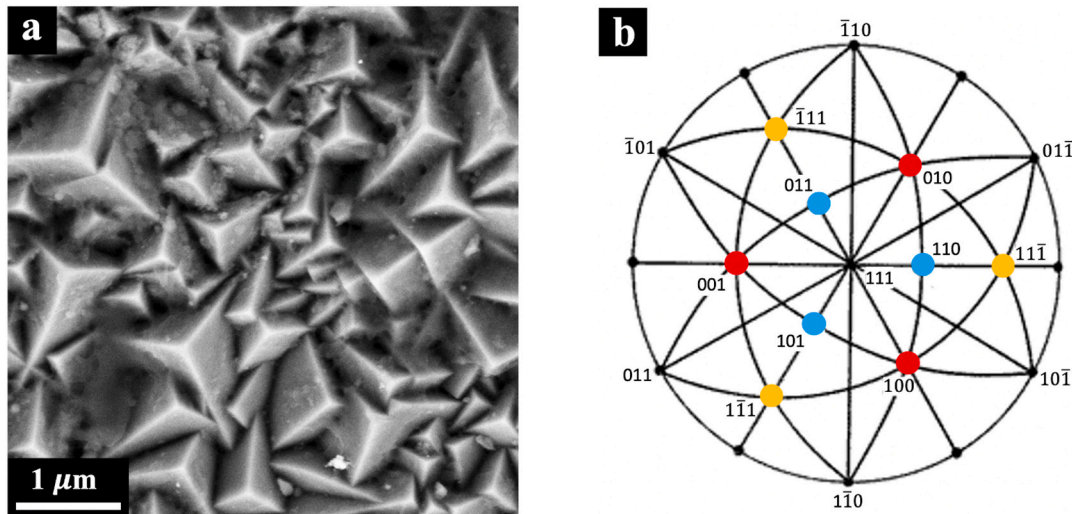


Fig. 4. (a) SEM SE image of the pyramid shape surface morphology of the 111 textured TiAlN coating. (b) Upper hemisphere of the 111 stereographic projection, where the possible facets of the grown pyramids are colored by blue, red and yellow.

of the TiAlN phase is identified in the diffractogram, due to a strong 111 texture. Similar to the sample A, no peak from the h-AlN phase above the background level could be found in the X-ray diffractogram of sample B. Cross sectional EBSD was measured from the sample B, and are presented in Fig. 9. The IPF map (along the coating growth direction) and the corresponding colour legend are shown in Fig. 9(a) and (b), the {100}, {110}, and {111} pole figures are shown in Fig. 9(c), (d), and (e), respectively. According to Fig. 9, the TiAlN grains in sample B also grow with a columnar morphology and a strong 111 texture. The columnar grains are seen in the STEM BF micrograph in Fig. 10(a). However, no nanolamella structure is found in this coating, instead a spatially homogeneous contrast in each grain can be observed. This absence of nanolamella can also be seen in the HRSTEM HAADF Z contrast micrograph in Fig. 10(b). The crystal structure of the TiAlN grains was found to be FCC also in this coating, as displayed in the indexed FFT in Fig. 10(c), which in addition reveals that the growth direction is close to [111] (upwards). In addition, the STEM XEDS measurement indicated a composition of around $\text{Ti}_{0.14}\text{Al}_{0.86}\text{N}$ in this coating (see Table 1), which is approximately the same as the Al(Ti)N in sample A where gas supply

rotation was applied.

In order to further study the influence of the rotational precursor supply, sample C was synthesized with a high gas supply rotation speed (see Table 1), see our previous paper [7]. This coating also has a pyramidal surface morphology, just as coatings A and B, see Fig. 7(b). The X-ray diffractogram of sample C is shown in Fig. 11. No peak of the h-AlN phase above the background level could be identified. The intense 111 peak indicates a strong 111 texture, just like for Samples A and B. As shown in Fig. 12(a), the TiAlN grains are composed of a nanolamella structure, but in sample C the periodicity is only ~ 9.5 nm, as can be seen in the image contrast line profile measured along the normal direction of the nanolamellae. The chemical compositions of the Ti(Al)N and the Al(Ti)N lamellae in sample C are similar to sample A, i.e. $\text{Ti}_{0.43}\text{Al}_{0.57}\text{N}$ and $\text{Ti}_{0.09}\text{Al}_{0.91}\text{N}$, respectively [7]. In addition, as shown by the HRSTEM HAADF micrograph and the corresponding FFT in Fig. 12(b) and (c), the epitaxial growth of the Ti(Al)N and the Al(Ti)N lamellae also follows the crystallographic orientation relationship reported above for sample A:

$$(001)_{\text{Ti(Al)N}} // (001)_{\text{Al(Ti)N}}, [010]_{\text{Ti(Al)N}} // [010]_{\text{Al(Ti)N}}.$$

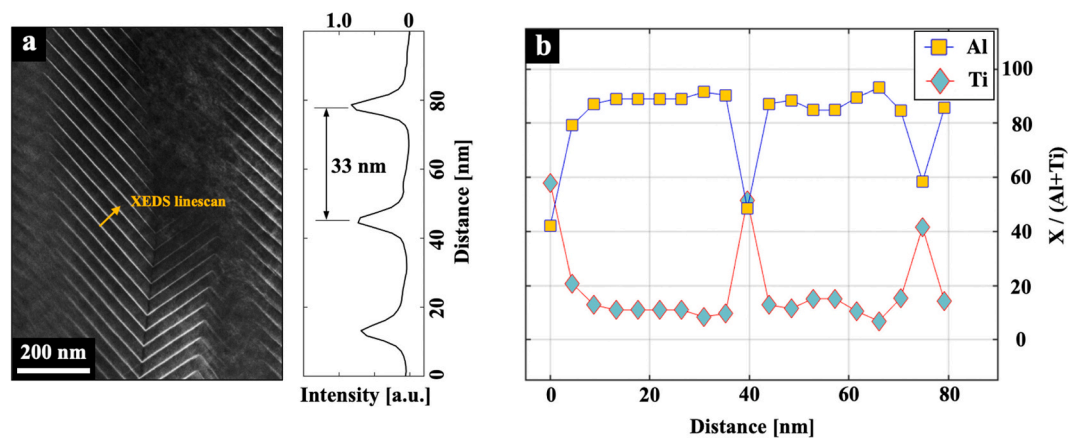


Fig. 5. Nanolamella structure of the TiAlN coating synthesized by slow rotation (sample A). (a) STEM HAADF micrograph of the nanolamella architecture where brighter lamellae are Ti rich and darker lamellae are Al rich. An image intensity line profile along the nanolamella normal direction is also presented. (b) Variation of Al and Ti contents along the nanolamella normal direction, obtained by STEM XEDS analysis. The location of XEDS linescan of (b) is indicated by the yellow arrow in (a).

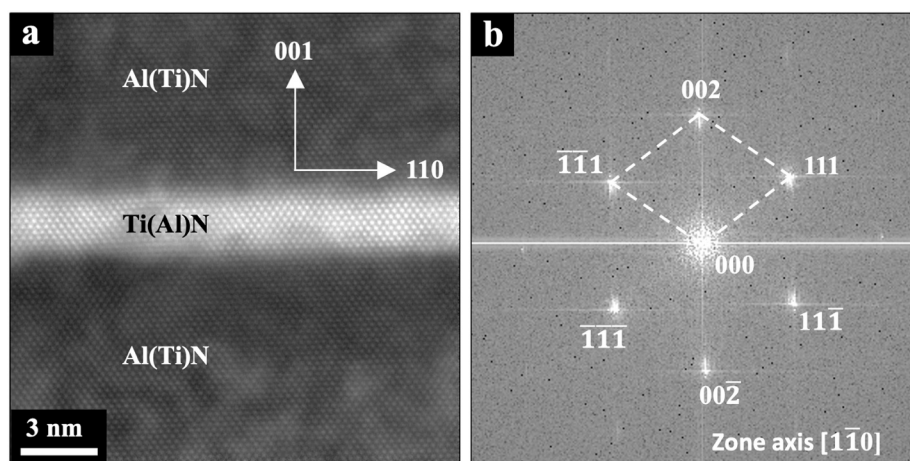


Fig. 6. Crystallographic orientation analysis of the nanolamellae based on HRSTEM HAADF imaging. (a) HRSTEM HAADF micrograph of nanolamella interfaces around Ti(Al)N. (b) FFT calculated from (a), illustrating the epitaxial growth of nanolamellae along the [001] direction (upwards).

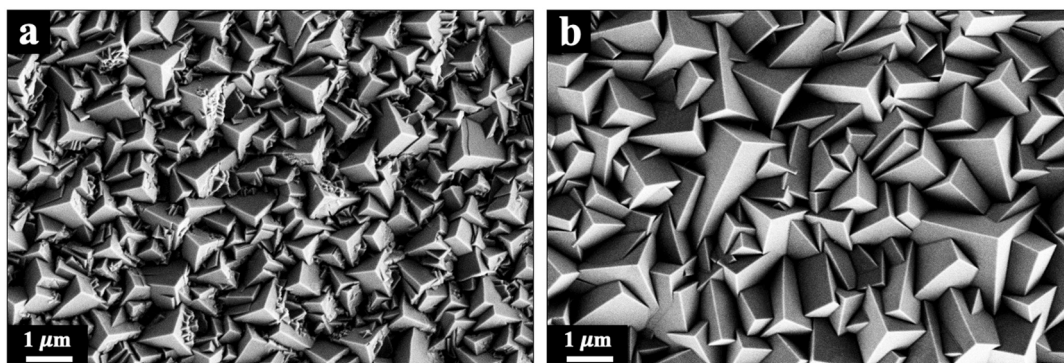


Fig. 7. SEM SE image of the pyramid shape surface morphology of (a) sample B, and (b) sample C.

EBSD measurements were done on sample C to investigate the presence of coating texture, and the results are presented in Fig. 13. Cross section EBSD mapping was carried out and the IPF map along the coating growth direction and the corresponding colour legend are shown in Fig. 13(a) and (b), respectively. Most grains have a 111

orientation, with occasional deviations of some grains. Thus, a 111 textured growth of columnar TiAlN grains is identified. This is also confirmed by EBSD pole figures, where a strong intensity along the coating growth direction is found for the {111} reflections, see Fig 13 (c–e).

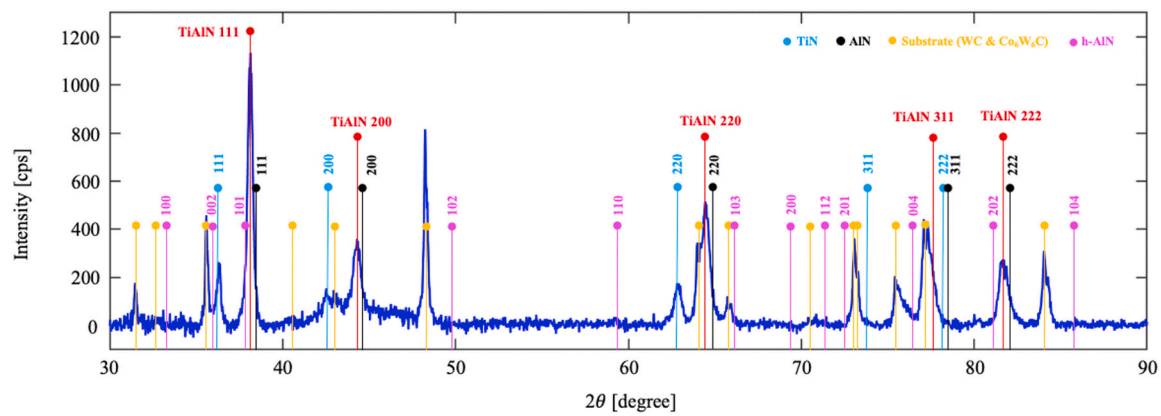


Fig. 8. X-ray diffractogram from sample B. The marked phases are (cubic) TiN (PDF 01-074-8388), (cubic) AlN (PDF 00-046-1200), WC (PDF 01-089-2727), and $\text{Co}_6\text{W}_6\text{C}$ (PDF 00-022-0597). Location of peaks from h-AlN (PDF 00-025-1133) are marked for reference.

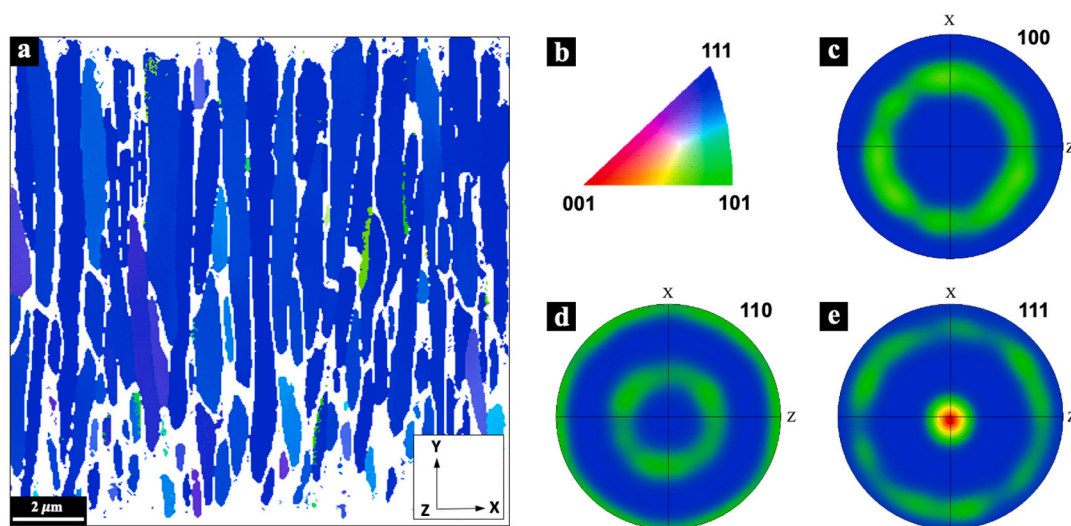


Fig. 9. EBSD results of the TiAlN coating synthesized by no rotation of the precursor supply (sample B). (a) IPF map of the coating cross section along the coating growth direction (vertically) showing the 111 texture. (b) Colour legend for the IPF map. (c–e) {100}, {110}, and {111} pole figures viewed along the coating growth direction confirming the 111 texture.

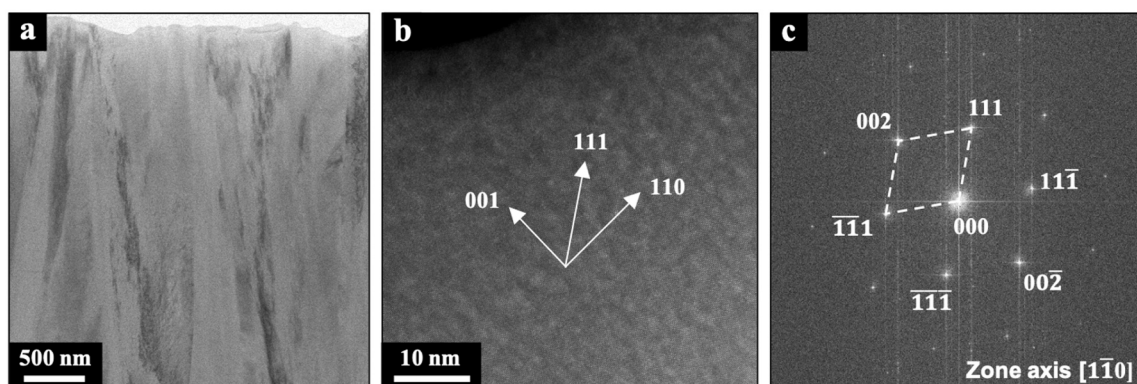


Fig. 10. TEM characterization of the TiAlN coating synthesized without rotation of gaseous precursor supply (sample B). (a) STEM BF micrograph of the coating cross section showing the columnar microstructure. (b) HRSTEM HAADF micrograph of a TiAlN grain showing the absence of nanolamellae. (c) FFT calculated from (b); the crystallographic orientations are marked, indicating a growth direction close to [111].

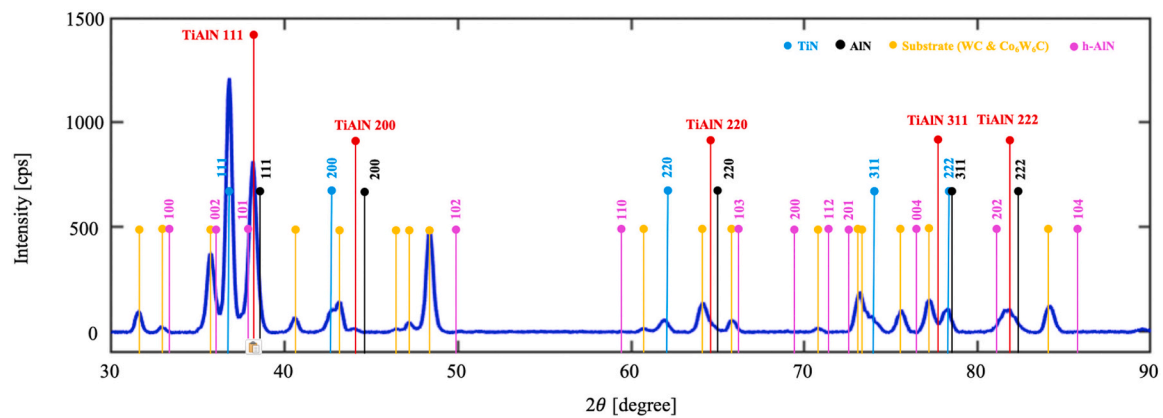


Fig. 11. X-ray diffractogram from sample C. The marked phases are (cubic) TiN (PDF 01-074-8388), (cubic) AlN (PDF 00-046-1200), WC (PDF 01-089-2727), and $\text{Co}_6\text{W}_6\text{C}$ (PDF 00-022-0597). Location of peaks from h-AlN (PDF 00-025-1133) are marked for reference.

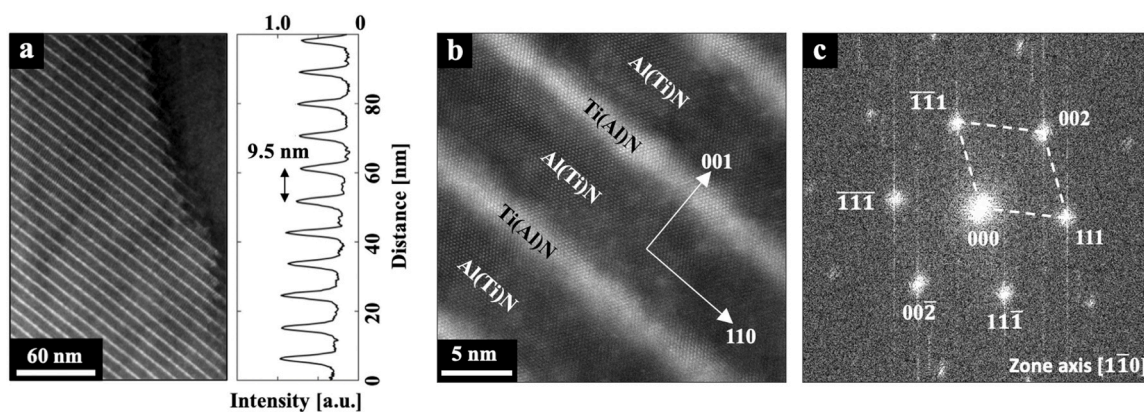


Fig. 12. Nanolamella structure of the TiAlN coating synthesized by fast gas supply rotation (sample C). (a) STEM HAADF micrograph showing the nanolamella structure in sample C with a periodicity of 9.5 nm. (b) HRSTEM HAADF micrograph of the nanolamella structure. (c) FFT calculated from (b) showing the local lamella alignment perpendicular to [001].

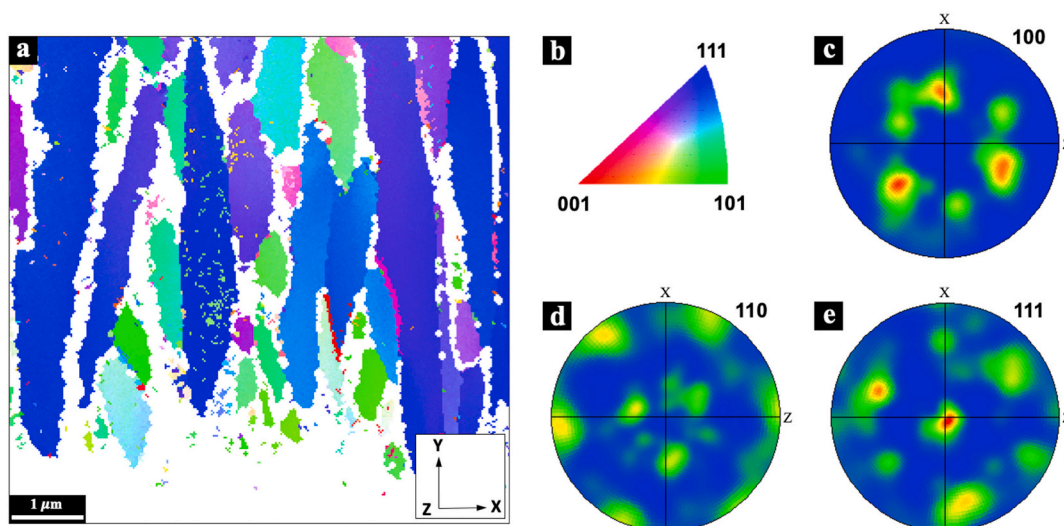


Fig. 13. EBSD results of the TiAlN coating synthesized by fast gas supply rotation (sample C). (a) IPF map of the coating cross section along the coating growth direction. (b) colour legend for the IPF map. (c–e) {100}, {110}, and {111} pole figures viewed along the coating growth direction.

4. Discussion

4.1. Coating texture and nanolamella epitaxial growth

The TiAlN coatings exhibit strong 111 texture and a pyramidal surface morphology with three facets. Candidates of atomic planes of the grown facets can, as described in Section 3.2, belong either to the {001}, {110}, or {111} planes. However, epitaxial growth of Ti(Al)N and Al(Ti)N nanolamellae (lying in the (001) plane) along the [001] direction was found. It thus indicates that the three pyramid sides (facets) are the three {001} planes, epitaxially growing with 3-fold rotational symmetry along the [111] direction, forming the nanolamella architecture on each of the three facets. Previously reported density functional theory (DFT) simulations indicate a noticeable lower surface energy for the {001} planes of TiAlN than for {111} and {110} planes [25]. The lower surface energy could therefore at least partly explain the formation of epitaxially grown nanolamellae on the {100} facets, although the growth is also kinetically driven. It is worth mentioning that both the Ti(Al)N and the Al(Ti)N nanolamellae observed in this work are thermodynamically metastable. Therefore, if the {001} facets are more stable than other facets, and the texture is 111, by symmetry this will lead to a pyramid shape of the TiAlN coatings.

According to references [10,12], it is especially difficult to obtain coatings with the cubic TiAlN phase with high Al content. Either it will not form or it can decompose and form h-AlN and TiN at elevated temperatures. For CVD grown metastable materials, the way that atoms are placed in the growing crystal is of importance for the metastability. This is influenced not only by the thermodynamics but also by the surface kinetics. This was shown for CVD growth of the metastable κ -Al₂O₃ by Yourdshahyan et al. [26]. For the TiAlN materials, it has been argued by Madan, et al. that a TiN layer can stabilize the metastable cubic AlN phase, although the stable range seemed to be limited to 2 nm [27]. In addition, Zalesak et al. suggested that the presence of the Ti(Al)N (Ti_{0.5}Al_{0.5}N) lamellae and the corresponding element non-stoichiometry are critical for stabilizing the cubic Al(Ti)N (Ti_{0.1}Al_{0.9}N) lamellae with high Al content [6]. However, in this work, the FCC TiAlN phase (sample B) was obtained also using a non-rotating gas supply, although without nanolamella architecture. Therefore, the Ti-rich phase (lamella) is not necessary for the formation of cubic TiAlN phase with high Al content, although the Ti-rich lamellae might have a stabilizing effect.

Both the nanolamella coatings (samples A and C), and the non-nanolamella coating (sample B) have strong 111 texture. This suggests that the texture formation in LPCVD TiAlN coatings is not influenced by the nanolamella architecture. In addition, TiAlN coatings with different nanolamella periodicities follow an identical cube-on-cube epitaxial growth of the Ti(Al)N and Al(Ti)N lamellae. Also, the chemical compositions of the Ti(Al)N and the Al(Ti)N lamellae are close, in the TiAlN coatings with different periodicities (samples A and C). Therefore, in our work, changing the spacing between neighbouring lamellae does not affect the crystallographic orientations or the chemical compositions in the nanolamella architecture.

4.2. Periodicity of nanolamella and rotational precursor gas supply

As shown in this work, the LPCVD TiAlN coatings synthesized with a rotational gas supply (samples A and C) contain periodic nanolamellae. Bartsch et al. proposed that an oscillating reaction happens in the CVD process, and causes temporal and local instabilities on the substrate surface [28]. By choosing suitable deposition conditions and alternating the gaseous precursors, the oscillatory controlled surface reaction in CVD enabled synthesis of Ti(N, C) and TiC-TiB₂ coatings with lamella architecture. Zalesak et al. also suggested that the nanolamella architecture formed in the TiAlN coatings results from oscillatory controlled surface reactions [6]. However, in this work, the TiAlN coating synthesized with a standing still gas supply (sample B) has no nanolamella present. This means that it is the rotational precursor supply, with

periodic variations in the incoming gas, that causes temporal varying surface reactions during the CVD process, which form the periodic nanolamella architecture. Although a composition fluctuation on the nanometer scale might exist in sample B, as indicated by the STEM HAADF micrograph in Fig. 10, this is more likely formed as a part of the deposition process itself, rather than as a spinodal decomposition of an initially homogeneous layer. Thus, spinodal decomposition is not likely to be the driving force behind nanolamella formation in LPCVD TiAlN.

As the nanolamella architecture is connected to the rotational gas supply, it is reasonable to assume that each rotation of the gas supply gives rise to one period of nanolamellae (one Al-rich, one Ti-rich). Based on this assumption, one can estimate the grown thickness in the macroscopic coating growth direction per gas supply rotation cycle (h_c in μm) to be:

$$h_c = \frac{v}{\omega} \quad (1)$$

where v is the coating growth rate (in $\mu\text{m}/\text{min}$), and ω is the gas supply rotation speed (in rpm), as shown in Table 1. As illustrated in Fig. 14(a), considering that the TiAlN coatings have a strong 111 texture, h_c is thus close to the growth distance along the [111] direction (h_{111}). The growth can further be correlated to the growth distances along the three <001> directions, i.e. the three facets growth directions (Fig. 4). Assuming the growth distance along e.g. the [001] direction, per gas supply rotation cycle, is equal to the nanolamella periodicity (λ in μm), we obtain:

$$\lambda = \frac{1}{\sqrt{3} \cos \alpha} h_c = \frac{1}{\sqrt{3} \cos \alpha} \frac{v}{\omega} \quad (2)$$

In Eq. (2), the factor $1/\sqrt{3}$ is a geometrical constant introduced due to the angle (54.7°) between nanolamellae normal direction [100] and the grain growth direction [111]. In addition, the TiAlN grain, from which the nanolamella period λ is measured, usually exhibits some inclination angle (α) between its [111] direction with respect to the coating growth direction (normal to the substrate surface), although the whole coating on average exhibits a 111 texture. Therefore, $1/\cos \alpha$ is a correction factor introduced due to the inclination of the grain. According to Eq. (2), the inverse nanolamella periodicity ($1/\lambda$), the factor of grain inclination angle ($\cos \alpha$), the gas supply rotation speed (ω) and the coating growth rate (v) follow:

$$\frac{1}{\lambda} = \sqrt{3} \cdot \cos \alpha \cdot \frac{\omega}{v} \quad (3)$$

According to Eq. (3), a linear relationship between $1/\lambda$ and $\cos \alpha \cdot \omega/v$ for the three samples is expected. The gas supply rotation speeds and coating growth rates for the samples A, B, and C are shown in Table 1. It was not possible to measure the inclination angle α for the specific columnar grain in which the periodicity λ was determined. Therefore, an average value of α was used, and this was calculated according to the cross section EBSD data (shown in Figs. 3, 9, and 13) that first had to be slightly re-aligned to 111 texture along the coating growth direction to correct the misalignment of sample during EBSD measurements (there is no reason to believe that a fiber texture should not be symmetric with respect to the surface normal). In this way, the average grain inclination angles for samples A, B, and C were determined to be 12° , 6° , and 14° , respectively. Fig. 14(b) shows the observed inverse nanolamella periodicities of samples A, B, and C (shown in Figs. 5, 10, and 12, respectively), which agree well with the values predicted according to Eq. (3). This thus supports the assumption that each gas supply rotation cycle creates one nanolamella period in the TiAlN coatings.

Of course, since the growth rate of sample B is about 9 times higher than sample A, it could be argued that no nanolamella forms in sample B due to lack of time for phase separation during a deposition with high growth rate. However, an increase of deposition rate by a factor of 3 (from sample A to sample C) gives no change in the nanolamella structure (the nanolamellae in samples A and C both look sharp and distinct), except for the nanolamella periodicity. A further increase of

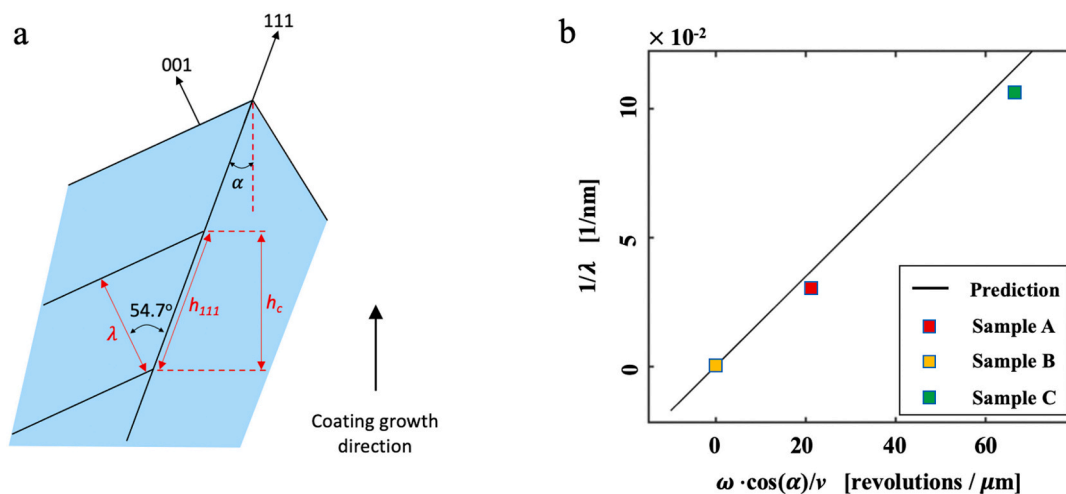


Fig. 14. Analysis of the nanolamella growth. (a) Schematic illustrating the relationship between the coating growth distance per gas supply rotation cycle (h_c) and the nanolamella periodicity along the [001] direction (λ); (b) comparison of the inverse nanolamella periodicity observed experimentally for samples A, B, and C, with the values predicted by Eq. (3), according to the gas supply rotation speed (ω), the coating growth rate (v) and the inclination angle (α).

the growth rate by a factor of 3 from sample C to sample B takes away the nanolamella architecture completely; there is no trace at all of nanolamella structure in sample B. Thus, it seems unlikely that the formation of the nanolamella structure depends on the growth rate. Instead, the clear connection to the gas supply rotation speed is evident.

In conclusion, each gas supply rotation cycle during the CVD process is believed to result in one period of the nanolamella architecture in samples A and C, including a thinner Ti(Al)N lamella and a thicker Al(Ti)N lamella. However, the process forming the Ti(Al)N and the Al(Ti)N lamellae during each gas supply rotation cycle will now be discussed. In a previous work [7] we studied the influence of the gas flow rate on the microstructure in an LPCVD TiAlN coating. At deposition conditions similar to those in this work we concluded that the Ti deposition is mass transport controlled, while the Al deposition is surface kinetically controlled, and it is important to keep the flow rate relatively low in order to produce TiAlN with high Al content.

Let us consider a schematic drawing representing the TiAlN deposition in the CVD reactor, see Fig. 15. When the beam of precursor gas

supply is directed towards the sample during a gas supply rotation cycle (Fig. 15(a)), the local gas velocity is high and forms a thin stagnant layer above the sample surface. This would lead to a higher Ti deposition rate, as it is mass transport controlled. This will create a Ti-rich layer (the Ti(Al)N lamellae). As illustrated in Fig. 15(b), when the gas beam rotates further away and does not hit the sample directly any more, the local gas flow rate becomes lower at the sample and a thicker stagnant layer is formed. Therefore, the deposition of Ti is suppressed and an Al-rich layer (the Al(Ti)N lamellae) is formed. During each gas supply rotation cycle, there is a shorter time when the gas beam directly hits the substrate or is in close enough proximity to generate sufficiently high local flow velocity, and a longer time with lower local gas velocity when the gas beam rotates away, i.e. the angle β (open angle of the precursors gas beam) is smaller than $360^\circ - \beta$. This produces a thinner Ti(Al)N lamella and a thicker Al(Ti)N lamella in each period of the nanolamella architecture, as illustrated in Fig. 15(c) and visible in the micrographs in Figs. 5, 6 and 12.

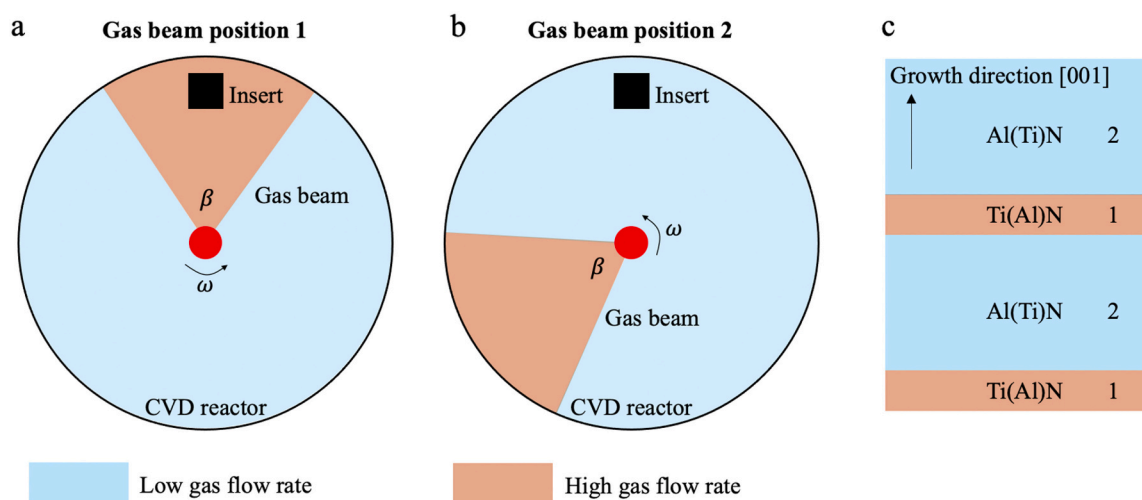


Fig. 15. Schematics of the proposed mechanism for the nanolamella architecture formation due to the rotational gas supply. (a) Gas beam position 1, where the precursor gas beam hits the sample substrate directly, creating a Ti(Al)N nanolamella. Angle β represents the opening range of the precursor gas beam. (b) Gas beam position 2, where the precursor gas beam rotates away, creating an Al(Ti)N nanolamella. (c) Iteratively grown Ti(Al)N and Al(Ti)N nanolamellae, corresponding to the gas beam positions 1 and 2, respectively.

5. Conclusions

In this work, we have shown that TiAlN coatings with or without nanolamella architecture can be deposited via LPCVD onto the cemented carbide cutting tool inserts pre-coated with a thin TiN layer. Based on our findings we come to the following conclusions:

- The TiAlN coatings have an FCC structure and consist of columnar grains with a pyramidal surface morphology with three {001} facets and a strong 111 texture.
- In the coatings produced by a rotating gas supply, the TiAlN grains are built up by nanolamellae parallel to the {001} facets. The lamellae are periodically grown $\text{Ti}_{0.5}\text{Al}_{0.5}\text{N}$ (Ti(Al)N) and $\text{Ti}_{0.1}\text{Al}_{0.9}\text{N}$ (Al(Ti)N), following a crystallographic orientation relationship as: $(001)_{\text{Ti(Al)N}} // (001)_{\text{Al(Ti)N}}$, $[010]_{\text{Ti(Al)N}} // [010]_{\text{Al(Ti)N}}$.
- The coating deposited without gas supply rotation still exhibited an FCC TiAlN structure, but without nanolamella. Thus, the presence of lamellae with lower Al-content (the Ti(Al)N/ $\text{Ti}_{0.5}\text{Al}_{0.5}\text{N}$ lamellae) was not necessary for the stabilization of the high Al-content (the Al(Ti)N/ $\text{Ti}_{0.1}\text{Al}_{0.9}\text{N}$ lamellae), although it cannot be excluded that such presence adds further stability.
- Spinodal decomposition is not likely to be the driving force behind the nanolamellae formation in LPCVD TiAlN, as this would have happened also in the sample without a rotational gas supply, producing nanolamellae, but it did not.
- The nanolamella architecture in the TiAlN coatings is revealed to originate from periodically varying surface reactions during the LPCVD process caused by the rotational gas supply of precursors, where each gas supply rotation cycle gives rise to one nanolamella period.
- The periodic formation of Ti(Al)N and Al(Ti)N lamellae is believed to be caused by the periodic variations of gas beam velocity and local gas partial pressures at the sample, leading to variations of the stagnant layer thickness and of species concentrations in the gas phase as well as on the surface. When the gas beam directly hits the sample, the Ti(Al)N lamella is formed, while when the gas beam rotates away the Al(Ti)N lamella is formed.
- The nanolamella periodicity (λ) is found to be directly influenced by the rotation speed (ω) of the precursors supply relative to the coating growth rate (v). Varying the gas supply rotation speed relative to the coating growth rate only changes the periodicity of nanolamellae in the TiAlN coating, but does not affect the crystallographic orientations, texture, or the chemical compositions in the nanolamella architecture.

CRediT authorship contribution statement

Ren Qiu: Conceptualization, Methodology, Validation, Formal analysis, Investigation, Writing – original draft, Visualization. **Olof Bäcke:** Investigation, Formal analysis, Writing – review & editing. **Dirk Stiens:** Conceptualization, Investigation, Formal analysis, Resources, Writing – review & editing. **Wiebke Janssen:** Investigation, Formal analysis, Writing – review & editing. **Johannes Kümmel:** Investigation, Formal analysis, Writing – review & editing. **Thorsten Manns:** Investigation, Formal analysis, Writing – review & editing. **Hans-Olof André:** Supervision, Formal analysis, Writing – review & editing. **Mats Halvarsson:** Conceptualization, Investigation, Formal analysis, Supervision, Project administration, Funding acquisition, Writing – review & editing.

Declaration of competing interest

The authors declare that they have no known competing financial interests or personal relationships that could have appeared to influence the work reported in this paper.

Acknowledgements

Funding from “CVD 2.0”, a Swedish Foundation for Strategic Research program via SSF contract RMA15-0048, is gratefully acknowledged. This research was mainly carried out at the Chalmers Materials Analysis Laboratory (CMAL).

References

- [1] J.M. Rodríguez, P. Jonsén, A. Svoboda, Simulation of metal cutting using the particle finite-element method and a physically based plasticity model, *Comput. Part. Mech.* 4 (2017) 35–51.
- [2] S. PalDey, S.C. Deevi, Single layer and multilayer wear resistant coatings of (Ti,Al)N: a review, *Mater. Sci. Eng. A* 342 (2003) 58–79.
- [3] R. Qiu, Electron Microscopy Investigation of Detailed Microstructures of CVD TiAlN and TiN Coatings - Effects of Gas Flow and Substrate on Coating Microstructure, Chalmers University of Technology, 2020.
- [4] M. to Baben, M. Hans, D. Primetzhofer, S. Evertz, H. Ruess, J.M. Schneider, Unprecedented thermal stability of inherently metastable titanium aluminum nitride by point defect engineering, *Mater. Res. Lett.* 5 (2017) 158–169.
- [5] K.M. Calamba, J. Salamaia, M.P.J. Jösaar, L.J.S. Johnson, R. Boyd, J.F. Pierson, M.A. Sortica, D. Primetzhofer, M. Odén, Effect of nitrogen vacancies on the growth, dislocation structure, and decomposition of single crystal epitaxial $(\text{Ti}_{1-x}\text{Al}_x)\text{N}_y$ thin films, *Acta Mater.* 203 (2021) 116509.
- [6] J. Zalesak, D. Holec, I. Matko, M. Petrevec, B. Sartory, N. Koutná, R. Daniel, R. Pitonak, J. Keckes, Peculiarity of self-assembled cubic nanolamellae in the TiN/AlN system: epitaxial self-stabilization by element deficiency/excess, *Acta Mater.* 131 (2017) 391–399.
- [7] R. Qiu, A. Forslund, O. Bäcke, A.H.S. Iyer, M. Sattari, W. Janssen, T. Manns, J. Kümmel, A. Ruban, D. Stiens, H.-O. André, M. Halvarsson, Effects of gas flow on detailed microstructure inhomogeneities in LPCVD TiAlN nanolamella coatings, *Materialia* 9 (2020) 100546.
- [8] J. Todt, J. Zalesak, R. Daniel, R. Pitonak, A. Köpf, R. Weißenbacher, B. Sartory, C. Mitterer, J. Keckes, Al-rich cubic $\text{Al}_{0.8}\text{Ti}_{0.2}\text{N}$ coating with self-organized nanolamellar microstructure: thermal and mechanical properties, *Surf. Coatings Technol.* 291 (2016) 89–93.
- [9] I. Endler, M. Höhn, M. Herrmann, R. Pitonak, S. Ruppi, M. Schneider, H. van den Berg, H. Westphal, Novel aluminum-rich $\text{Ti}_{1-x}\text{Al}_x\text{N}$ coatings by LPCVD, *Surf. Coatings Technol.* 203 (2008) 530–533.
- [10] A. Kimura, H. Hasegawa, K. Yamada, T. Suzuki, Metastable $\text{Ti}_{1-x}\text{Al}_x\text{N}$ films with different Al content, *J. Mater. Sci. Lett.* 19 (2000) 601–602.
- [11] M. Zhou, Y. Makino, M. Nose, K. Nogi, Phase transition and properties of Ti–Al–N thin films prepared by r.f.-plasma assisted magnetron sputtering, *Thin Solid Films* 339 (1999) 203–208.
- [12] U. Wahlström, L. Hultman, J.E. Sundgren, F. Adibi, I. Petrov, J.E. Greene, Crystal growth and microstructure of polycrystalline $\text{Ti}_{1-x}\text{Al}_x\text{N}$ alloy films deposited by ultra-high-vacuum dual-target magnetron sputtering, *Thin Solid Films* 235 (1993) 62–70.
- [13] Ben Hassine M., Andren H.-O., Iyer A.H.S., Lostsari A., Bäcke O., Stiens D., Janssen W., Manns T., Kümmel J., Halvarsson M., Growth model for high-Al containing CVD TiAlN coatings on cemented carbides using intermediate layers of TiN, submitted for publication (2021).
- [14] F. Uny, S. Achache, S. Lamri, J. Ghanbaja, E. Fischer, M. Pons, E. Blanquet, F. Schuster, F. Sanchette, Deposition and characterization of (Ti, Al)N coatings deposited by thermal LPCVD in an industrial reactor, *Surf. Coatings Technol.* 358 (2019) 923–933.
- [15] P.M. Anderson, C. Li, Hall-Petch relations for multilayered materials, *Nanostructured Mater.* 5 (1995) 349–362.
- [16] L. Geyang, H. Zenghu, T. Jiawan, X. Junhua, G. Mingyuan, Alternating stress field and superhardness effect in TiN/NbN superlattice films, *J. Vac. Sci. Technol. A* 20 (2002) 674–677.
- [17] S. Subedi, I.J. Beyerlein, R. LeSar, A.D. Rollett, Strength of nanoscale metallic multilayers, *Scr. Mater.* 145 (2018) 132–136.
- [18] H. Caliskan, E. Altas, P. Panjan, Study of nanolayer AlTiN/TiN coating deposition on cemented carbide and its performance as a cutting tool, *J. Nano Res.* 47 (2017) 1–10.
- [19] C. Ducros, V. Benevent, F. Sanchette, Deposition, characterization and machining performance of multilayer PVD coatings on cemented carbide cutting tools, *Surf. Coatings Technol.* 163–164 (2003) 681–688.
- [20] Y.X. Xu, L. Chen, F. Pei, K.K. Chang, Y. Du, Effect of the modulation ratio on the interface structure of TiAlN/TiN and TiAlN/ZrN multilayers: first-principles and experimental investigations, *Acta Mater.* 130 (2017) 281–288.
- [21] H. Holleck, V. Schier, Multilayer PVD coatings for wear protection, *Surf. Coatings Technol.* 76–77 (1995) 328–336.
- [22] A. Knutsson, M.P. Johansson, L. Karlsson, M. Odén, Thermally enhanced mechanical properties of arc evaporated $\text{Ti}_{0.34}\text{Al}_{0.66}\text{N}$ /TiN multilayer coatings, *J. Appl. Phys.* 108 (2010) 44312.
- [23] A. Paseuth, K. Yamagata, A. Miura, M. Higuchi, K. Tadanaga, M. Cinibulk, Deposition and analysis of Al-rich $\text{c-Al}_x\text{Ti}_{1-x}\text{N}$ coating with preferred orientation, *J. Am. Ceram. Soc.* 100 (2016) 343–353.
- [24] D. Stiens, T. Manns, S. Ruppi, TiAlCN layers with lamellae structure, US patent 10,214,810 B2, 2019.

- [25] A. Forslund, A. Ruban, Surface energetics of $\text{Al}_x\text{Ti}_{1-x}\text{N}$ alloys, *Comput. Mater. Sci.* 183 (2020) 109813.
- [26] Y. Yourdshahyan, C. Ruberto, M. Halvarsson, L. Bengtsson, V. Langer, B. I. Lundqvist, S. Rупpi, U. Rolander, Theoretical structure determination of a complex material: $\kappa\text{-Al}_2\text{O}_3$, *J. Am. Ceram. Soc.* 82 (1999) 1365–1380.
- [27] A. Madan, I.W. Kim, S.C. Cheng, P. Yashar, V.P. Dravid, S.A. Barnett, Stabilization of cubic AlN in epitaxial AlN/TiN superlattices, *Phys. Rev. Lett.* 78 (1997) 1743–1746.
- [28] K. Bartsch, A. Leonhardt, E. Wolf, Deposition of multilayer hard coatings using kinetically controlled chemical vapour deposition processes, *Surf. Coatings Technol.* 54–55 (1992) 193–197.